Nanoscale Electronic Inhomogeneity in In₂Se₃ Nanoribbons Revealed by Microwave Impedance Microscopy

Keji Lai,[†,‡] Hailin Peng,[†,§] Worasom Kundhikanjana,[‡] David T. Schoen,[§] Chong Xie,[§] Stefan Meister,[§] Yi Cui,*[,§] Michael A. Kelly,[§] and Zhi-Xun Shen*[,‡]

Department of Applied Physics and Department of Materials Science and Engineering, Stanford University, Stanford, California 94305

Received January 21, 2009

ABSTRACT

Driven by interactions due to the charge, spin, orbital, and lattice degrees of freedom, nanoscale inhomogeneity has emerged as a new theme for materials with novel properties near multiphase boundaries. As vividly demonstrated in complex metal oxides (see refs 1−5) and chalcogenides (see refs 6 and 7), these microscopic phases are of great scientific and technological importance for research in high-temperature superconductors (see refs 1 and 2), colossal magnetoresistance effect (see ref 4), phase-change memories (see refs 5 and 6), and domain switching operations (see refs 7−9). Direct imaging on dielectric properties of these local phases, however, presents a big challenge for existing scanning probe techniques. Here, we report the observation of electronic inhomogeneity in indium selenide (In₂Se₃) nanoribbons (see ref 10) by near-field scanning microwave impedance microscopy (see refs 11−13). Multiple phases with local resistivity spanning 6 orders of magnitude are identified as the coexistence of superlattice, simple hexagonal lattice and amorphous structures with ~100 nm inhomogeneous length scale, consistent with high-resolution transmission electron microscope studies. The atomic-force-microscope-compatible microwave probe is able to perform a quantitative subsurface electrical study in a noninvasive manner. Finally, the phase change memory function in In₂Se₃ nanoribbon devices can be locally recorded with big signals of opposite signs.

While the conventional wisdom on solids largely results from the real-space periodic structures and k-space band theories,[14] recent advances in physics have shown clear evidence that microscopic inhomogeneity, manifested as submicrometer spatial variations of the material properties, could indeed occur under certain conditions. Utilizing various probe−sample coupling mechanisms,[15] spatial inhomogeneity has been observed as nanometer gap variations in high-Tc superconductors,[1,2] coexisting electronic states in VO_2 near the metal−insulator transition,[3] ferromagnetic domains in manganites showing colossal magnetoresistance effect,[4] and in an ever-growing list. Probing these nonuniform phases provides not only much knowledge of the underlying interactions but also valuable information for applications of the domain structures. In particular, spatially resolved properties are of significant interest for phase change and other switching materials to be on board the nanoelectric era.[5−9]

While a number of contrast mechanisms[15] (Figure S1 in Supporting Information) have been employed to visualize the electronic inhomogeneity, established scanning probe techniques do not directly access the low-frequency (f) complex permittivity $\varepsilon(\omega) = \varepsilon' + i\sigma/\omega$, where ε' is the dielectric constant and σ the conductivity, which holds a special position to study the ground-state properties of materials. For local electrodynamic response, a near-field technique is imperative to resolve spatial variations at length scales well below the radiation wavelength.[16] For this study, the working frequency is set at ~1 GHz, i.e., in the microwave regime, to stay below resonant excitations at optical frequencies.[17] The near-field interaction can be understood as tip−sample impedance change. And a thin surface insulating layer, equivalent to small series impedance, will not shield the capacitive coupling to subsurface features. The ac detection is very sensitive using mostly noninvasive rf excitation (<0.1 V), in contrast to electrostatic probes[15] requiring a high dc bias (>1 V) to reveal the conductivity distribution.

The most common design of the near-field microwave probe is an etched metal tip, which limits the resolution to several micrometers, backed by a massive cavity or transmission line resonator.[18−20] The strong contact force due to the rigid structure easily causes damage to the tip and the sample, halting the applications on practical nanodevices. Compliant cantilever probes on atomic force microscope (AFM) plat-

* Correspondence and requests for materials should be addressed to Z.X.S. (zxshen@stanford.edu) or Y.C. (yicui@stanford.edu).
† These authors contributed equally to this work.
‡ Department of Applied Physics.
§ Department of Materials Science and Engineering.
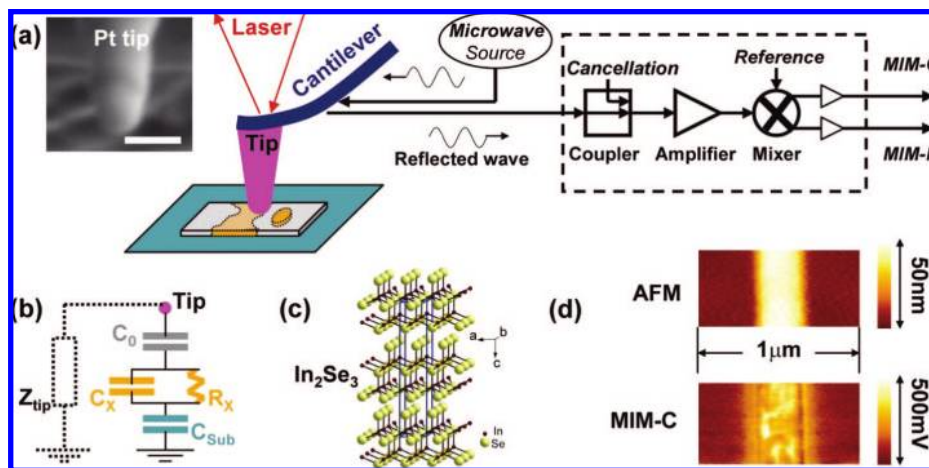
Figure 1. (a) Schematic of the cantilever-based MIM system setup. Surface topography is simultaneously obtained by the AFM laser feedback. The microwave electronics suppress the background of the reflected microwave signal and detect the changes during the scanning. The two mixer outputs are recorded to form MIM-C and MIM-R images. The inset SEM picture shows the Pt tip deposited by a FIB, and the scale bar is 200 nm. (b) A circuit model of the tip−sample interaction, shown as a lumped-element load in parallel with the tip impedance Z_{tip}. The surface layer and the substrate are both dielectrics and represented by capacitors C_0 and C_{sub}. The In_2Se_3 sample with finite conductivity is described as two components C_X and R_X in parallel. (c) Layered crystal structure of bulk In_2Se_3. (d) Simultaneously taken topography and MIM-C images of an In_2Se_3 nanoribbon. The resistance across this device is 2 MΩ. The microwave image reveals clear electronic inhomogeneity, while the AFM image shows essentially a flat surface.

forms[21] (Figure 1a) are much better in this aspect. In this work, the probe of our scanning microwave impedance microscope (MIM) is microfabricated on silicon nitride cantilevers with shielded metal traces and focused-ion beam (FIB) deposited Pt tip[11−13] (Figure 1a inset). The microwave electronics detect the real and imaginary components of the effective tip−sample impedance and output as MIM-R and MIM-C signals (Figure 1b), which contain the local (ε,σ) information of the material. Therefore, we believe that the MIM can afford a powerful and general-purpose tool to study nanoscale dielectric inhomogeneity in a noninvasive manner.

The material for this study is the layer-structured III−VI compound In_2Se_3, a technologically important system in solar cells,[22] batteries,[23] and phase-change random access memory (PRAM)[24,25] applications. The crystal structure, as seen in Figure 1c, shows strong covalent bonding within each layer and a weak van der Waals force between the layers. While bulk In_2Se_3 presents many complicated crystal structures,[26] the nanostructures grown by the vapor−liquid−solid (VLS) method is single-crystalline in nature.[27,28] The nanoribbon samples, with a thickness $t = 20−50$ nm and a width varying from 100 nm to several micrometers, were transferred to SiN_x substrates and contacted by In/Au electrodes.[10] Figure 1d shows the MIM image of an In_2Se_3 nanoribbon. While the standard AFM signal shows a flat surface, the MIM-C image reveals clear submicrometer spatial inhomogeneity. A collection of microwave images of In_2Se_3 samples can be found in Figure S2 in the Supporting Information. Throughout the paper, the color rendering is such that brighter color represents larger tip−sample capacitance in MIM-C and more loss in MIM-R.

A careful study of the microwave images was performed on a large In_2Se_3 nanoribbon piece contacted by four In/Au electrodes, as seen from the scanning electron microscope (SEM) picture and AFM image in Figure 2a. Voltage pulses
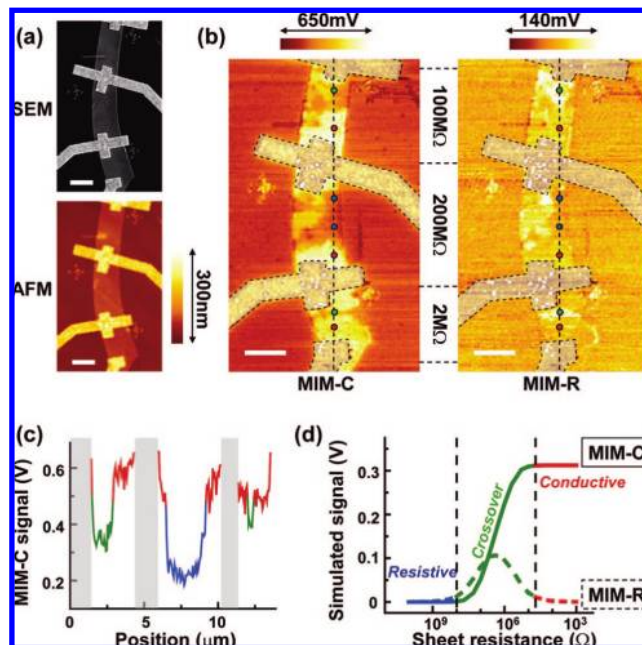
Figure 2. (a) SEM (top) and AFM (bottom) images of a large In_2Se_3 nanoribbon. (b) MIM-C (left) and MIM-R (right) images of the same ribbon, with the electrodes masked. The resistances of the three segments (top-down) are 100, 200, and 2 MΩ, respectively. A dashed line across the ribbon is plotted and labeled by red, green, and blue dots. All scale bars in (a) and (b) are 2 μm. (c) A line cut of the MIM-C image in (b) (electrodes excluded). (d) Simulated MIM-C (solid line) and MIM-R (dashed line) signals as a function of the local sheet resistance. The black dashed lines roughly mark the boundaries of different regimes. The MIM-C signal increases monotonically with reducing sheet resistance, while the MIM-R signal peaks around 2 MΩ/square in the crossover region. (b), (c), and (d) are color coded such that red is used for highly conductive, green for intermediate, and blue for highly resistive areas.

were applied across these leads to induce appreciable conductivity inhomogeneity. After the pretreatment, the two-

terminal resistances (R_{2T})[29] of all three segments increased by 3 decades (Figure S3 in Supporting Information). Using the standard conductive AFM (C-AFM) mode, we also confirmed that the sample surface is insulating and prohibits dc current flow (Figure S4 in Supporting Information).

The MIM images of the same ribbon are shown in Figure 2b, with the data on the metal electrodes excluded in the analysis (Figure S5 in Supporting Information). Substantial electronic inhomogeneity is observed within the nanoribbon, which cannot be resolved by SEM, AFM, or C-AFM. Qualitatively, the near-field response is consistent with the transport data between adjacent electrodes. For the upper two sections with R_{2T} in the order of 10^8 Ω, the MIM images display strong nonuniformity. Whereas for the bottom section with $R_{2T} = 2$ MΩ, the bright area dominates the MIM-C image except for a weak breakage in the middle. The length scale of these inhomogeneous domains ranges from 100 nm to μm. The sharpest transition between different domains is ~100 nm, as seen in the line cut in Figure 2c, which is equivalent to the tip diameter.

Quantitative understanding of the images requires finite-element analysis (FEA) of the tip−sample interaction,[12] and the result is shown in Figure 2c. Details of the simulation, which explicitly considers the finite thickness and width of the In$_2$Se$_3$ nanoribbons, are found in Figure S6 in the Supporting Information. For illustration purpose, the x-axis is converted to local sheet resistance $R_S = 1/(\sigma t)$ and y-axis to output voltage, with 1 GΩ^{-1} admittance (inverse imped-ance) contrast corresponding to ~1.5 mV signal. For decreasing R_S, the MIM-C signal stays low in the resistive limit ($R_S > 10^8$ Ω), rises monotonically in the crossover regime (10^8 $\Omega > R_S > 10^5$ Ω), and finally saturates[30] in the conductive limit ($R_S < 10^5$ Ω). The MIM-R signal, on the other hand, peaks around $R_S = 2$ MΩ, where the loss is significant, and vanishes at both extremes. The simulation is in excellent agreement with the data. For example, along the vertical line cut in parts b and c of Figure 2, the red dots mark the highly conductive regions, which are indeed bright in MIM-C and faint in MIM-R. The blue dots label the highly resistive areas with little contrast over the substrate in both channels. Two regions, bright in MIM-R but dim in MIM-C, are indicated by green dots. In particular, such intermedi-ate-σ feature traverses the entire ribbon between the bottom two electrodes, where $R_{2T} \sim 2$ MΩ coincides with the crossover R_S in Figure 2c. Interestingly, the highly conductive regions are mostly found near the In/Au electrodes, which may indicate that the Joule heating first destroys the metallic phase away from the Ohmic contacts. Finally, the maximum contrast signal, ~300 mV in MIM-C and ~100 mV in MIM-R, also agrees with the lumped-element FEA simulation.

In order to shed some light on the observed electronic inhomogeneity, control experiments were carried out on In$_2$Se$_3$ nanoribbons deposited on SiN$_x$ membranes for simultaneous transmission electron microscope (TEM) and transport studies.[10] Three distinct structural phases, as seen from the high-resolution TEM images and the selected-area electron diffraction (SAED) patterns in Figure 3a, are observed in ribbons in the [11$\bar{2}$0] growth direction. Cor-
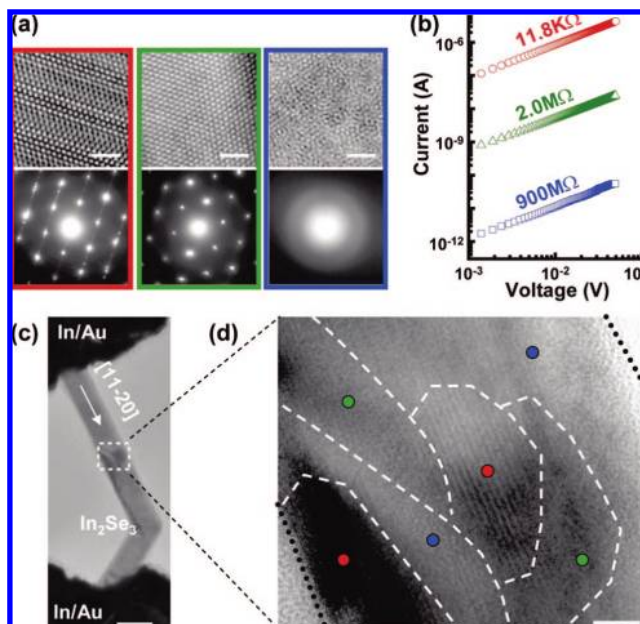

Figure 3. (a) High-resolution transmission electron microscopy (HRTEM) images (top) and the corresponding selected-area electron diffraction (SAED) patterns (bottom). The structures from left to right correspond to superlattice, simple hexagonal lattice, and amorphous phases. All scale bars are 2 nm. (b) Typical $I-V$ characteristics of three different states of [11$\bar{2}$0] In$_2$Se$_3$ nanoribbons. (c) Low-resolution TEM image of an In$_2$Se$_3$ nanoribbon device on SiN$_x$ membrane. The scale bar is 100 nm. (c) Zoom-in HRTEM image of the selected area in (c). The scale bar is 10 nm. The black dotted lines show the boundaries of the ribbon. The dashed white lines roughly mark the boundaries between different domains. The color scheme (red, green, and blue) is the same as that used in Figure 2.

respondingly, typical $I-V$ characteristics of the three phases are shown in Figure 3b. It has been previously reported that pristine VLS-grown [11$\bar{2}$0] In$_2$Se$_3$ nanoribbons with super-lattice structures (Figure 3a, left) exhibit metallic behavior and room temperature R_{2T} as low as kiloohms.[10] Further studies show that after applying a low voltage (<1 V) pulse, R_{2T} can increase up to megaohms and the ribbons behave semiconducting (Figure S7 in Supporting Information). For these devices, the superlattice structure is usually lost and a simple hexagonal lattice is observed (Figure 3a, middle). Finally, as a phase change material,[24,25] In$_2$Se$_3$ can be switched between crystalline and amorphous (Figure 3a, right) states by high voltage pulses, with R_{2T} in the gigaohms range for the amorphous state. Interestingly, all three phases could coexist in a single device after Joule heating, as seen in Figure 3c and the zoom-in view in Figure 3c. The length scale of this structural inhomogeneity is again around 50−100 nm. We therefore assign the same color scheme (red, green, and blue) here in accordance with the local electrical imaging result in Figure 2.

Finally, we demonstrate that the MIM can provide spatially resolved information when In$_2$Se$_3$ nanodevices are phase-switched by voltage pulses. Figure 4a shows the SEM image of a long nanoribbon contacted by 9 In/Au leads. The resistance between adjacent fingers was around 10 kΩ before any treatment. For the intact segment iii below the bottom-
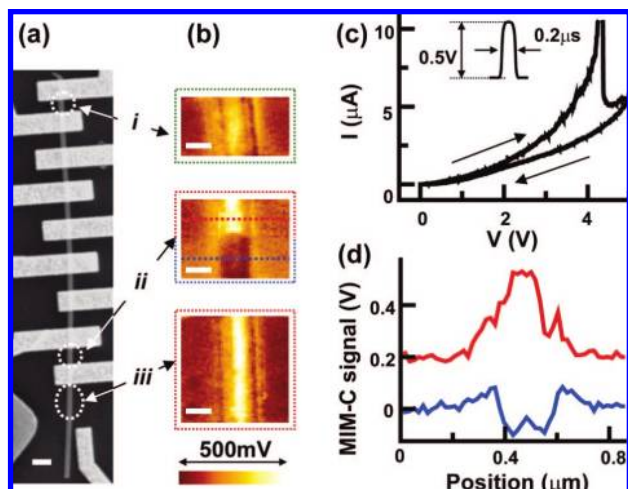
Figure 4. (a) SEM image of a long In$_2$Se$_3$ nanoribbon, 200 nm in width and 30 nm in thickness, with multiple contacts. The scale bar is 1 μm. (b) MIM-C images of three segments, labeled as i, ii, and iii in (a), of the same ribbon. The scale bars are 200 nm. (c) $I-V$ curve of a high voltage sweep on segment ii. For the up-sweep, the current increased above 10 μA at around 4 V bias and suddenly dropped to 5 μA. The down-sweep then followed completely different characteristics. The inset shows a low voltage (0.5 V) pulse applied on the nanoribbon before this sweep. (c) Two line cuts of the MIM-C image ((b)) of segment ii, showing two domains with opposite contrast over the background. The red line is shifted upward by 0.2 V for clarity. Again, the color coding (red, green, and blue) is in accordance with that in Figures 2 and 3.

most electrode, the MIM-C image in Figure 4b (bottom) appears very bright over the substrate. In the successive transport measurements, short pulses, depicted in the inset of Figure 4c, were applied to the ribbon and R_{2T} increased to >1 MΩ for all sections. After this pulse, the MIM-C image shows a much weaker contrast over the background, as seen for section i (Figure 4b, top) with $R_{2T} = 2$ MΩ. Furthermore, a high bias sweep (Figure 4c) was applied across the nanoribbon segment ii. Interestingly, the MIM-C data of this segment (Figure 4b, middle) clearly break into two domains. The upper portion of the device shows positive contrast over the background and the lower portion negative (Figure S6 in Supporting Information). We therefore conclude that as the device cooled down from the melting point, the upper part recrystallized and became highly conductive again, while the lower part stayed amorphous and resistive. We note that the large signal with opposite signs recorded by the MIM (Figure 4c) most vividly displays the phase change memory function of the In$_2$Se$_3$ devices. It is possible to further implement the MIM as a spatially resolved readout instrument for memories with large resistivity changes. Rather than detecting the minute topographical variations accompanying the phase change,[6] the MIM directly measures the local electronic property and is much more sensitive for the operation.

Supporting Information Available: Comparison of various electrical probes, additional microwave images showing electronic inhomogeneity, effect of external voltage pulses, conductive AFM result, image process in the presence of metal electrodes, simulation using finite-element analysis software, and metallic vs insulating temperature dependence. This material is available free of charge via the Internet at http://pubs.acs.org.

References

(1) Pan, S. H.; O'Neal, J. P.; Badzey, R. L.; Chamon, C.; Ding, H.; Engelbrecht, J. R.; Wang, Z.; Eisaki, H.; Uchida, S.; Gupta, A. K.; Ng, K. W.; Hudson, E. W.; Lang, K. M.; Davis, J. C. *Nature* **2001**, *413*, 282–285.
(2) McElroy, K.; Lee, J.; Slezak, J. A.; Lee, D. H.; Eisaki, H.; Uchida, S.; Davis, J. C. *Science* **2005**, *309*, 1048–1052.
(3) Qazilbash, M. M.; Brehm, M.; Chae, B.-G.; Ho, P. C.; Andreev, G. O.; Kim, B.-J.; Yun, S. J.; Balatsky, A. V.; Maple, M. B.; Keilmann, F.; Kim, H.-T.; Basov, D. N. *Science* **2007**, *318*, 1750–1753.
(4) Dagotto, E. *Nanoscale phase separation and colossal magnetoresistance: the physics of manganites and related compounds*; Springer: New York, 2002.
(5) Wu, J.; Gu, Q.; Guiton, B. S.; de Leon, N. P.; Ouyang, L.; Park, H. *Nano Lett.* **2006**, *6*, 2313–2317.
(6) Hamann, H. F.; O'Boyle, M.; Martin, Y. C.; Rooks, M.; Wickramasinghe, H. K. *Nat. Mater.* **2006**, *5*, 383–387.
(7) Terabe, K.; Hasegawa, T.; Nakayama, T.; Aono, M. *Nature* **2005**, *433*, 47–50.
(8) Szot, K.; Speier, W.; Bihlmayer, G.; Waser, R. *Nat. Mater.* **2006**, *5*, 312–320.
(9) Jesse, S.; Rodriguez, B. J.; Choudhury, S.; Baddorf, A. P.; Vrejoiu, I.; Hesse, D.; Alexe, M.; Eliseev, E. A.; Morozovska, A. N.; Zhang, J.; Chen, L.-Q.; Kalinin, S. V. *Nat. Mater.* **2008**, *7*, 209–215.
(10) Peng, H.; Xie, C.; Schoen, D. T.; Cui, Y. *Nano Lett.* **2008**, *8*, 1511–1516.
(11) Lai, K.; Ji, M. B.; Leindecker, N.; Kelly, M. A.; Shen, Z. X. *Rev. Sci. Instrum.* **2007**, *78*, 063702.
(12) Lai, K.; Kundhikanjana, W.; Kelly, M.; Shen, Z. X. *Rev. Sci. Instrum.* **2008**, *79*, 063703.
(13) Lai, K.; Kundhikanjana, W.; Kelly, M. A.; Shen, Z. X. *Appl. Phys. Lett.* **2008**, *93*, 123105.
(14) Ashcroft, N. W.; Mermin, N. D. *Solid State Phys.*; Thomson Learning, 1976.
(15) Meyer, E.; Hug, H.; Bennewitz, R. *Scanning probe microscopy: the lab on a tip*; Springer: Berlin, 2003.
(16) Rosner, B. T.; van der Weide, D. W. *Rev. Sci. Instrum.* **2002**, *73*, 2505–2525.
(17) Hillenbrand, R.; Taubner, T.; Keilmann, F. *Nature* **2002**, *418*, 159–162.
(18) Wei, T.; Xiang, X.-D. *Appl. Phys. Lett.* **1996**, *68*, 3506–3508.
(19) Tabib-Azar, M.; Su, D. P.; Pohar, A.; LeClair, S. R.; Ponchak, G. *Rev. Sci. Instrum.* **1999**, *70*, 1725–1729.
(20) Alexander, T.; Steven, M. A.; Hans, M. C.; Robert, L. M.; Vladimir, V. T.; Andrew, R. S. *Rev. Sci. Instrum.* **2003**, *74*, 3167–3170.
(21) Massood, T.-A.; Yaqiang, W. *IEEE Trans. Microwave Theory Tech.* **2004**, *52*, 971–979.
(22) Kwon, S. H.; Ahn, B. T.; Kim, S. K.; Yoon, K. H.; Song, J. *Thin Solid Films* **1998**, *323*, 265–269.
(23) Julien, C.; Hatzikraniotis, E.; Chevy, A.; Kambas, K. *Mater. Res. Bull.* **1985**, *20*, 287–292.
(24) Lee, H.; Kang, D. H.; Tran, L. *Mater. Sci. Eng., B* **2005**, *119*, 196–201.

(25) Yu, B.; Ju, S. Y.; Sun, X. H.; Ng, G.; Nguyen, T. D.; Meyyappan, M.; Janes, D. B. *Appl. Phys. Lett.* **2007**, *91*, 133119.

(26) Ye, J. P.; Soeda, S.; Nakamura, Y.; Nittono, O. *Jpn. J. Appl. Phys., Part 1* **1998**, *37*, 4264–4271.

(27) Peng, H. L.; Schoen, D. T.; Meister, S.; Zhang, X. F.; Cui, Y. *J. Am. Chem. Soc.* **2007**, *129*, 34–35.

(28) Two different growth directions, [0001] and [11$\bar{2}$0], are found in our VLS-grown In$_2$Se$_3$ nanostructures. For simplicity, we only discuss the results of nanoribbons with [11$\bar{2}$0] growth direction, i.e., perpendicular to the normal direction of the layers.

(29) Only R_{2T} is reported in the paper because the resistance of In$_2$Se$_3$ ribbons spans many orders of magnitude. For metallic ribbons, four-terminal measurements were also performed and it is confirmed that the In/Au contact resistance is small (<1 kΩ) compared with the sample resistance.

(30) Wang, Z.; Kelly, M. A.; Shen, Z.-X.; Shao, L.; Chu, W.-K.; Edwards, H. *Appl. Phys. Lett.* **2005**, *86*, 153118.

NL900222J